ADVANCED ELECTRONIC MATERIALS
Open Access
www.advelectronicmat.de

# Weyl Fermion Manipulation Through Magnetic Transitions in the Ferromagnetic Non-Centrosymmetric Weyl Semimetal PrAlSi

*Kaipu Wang, Wujun Shi,* Weizheng Cao, Xiaotian Yang, Zhengyang Lv, Cheng Peng, Cheng Chen, Defa Liu, Haifeng Yang, Lexian Yang, Meng Lyu, Peijie Sun, Enke Liu, Mao Ye, Yulin Chen, Yan Sun, Yanpeng Qi,* and Zhongkai Liu**

**PrAlSi, a non-centrosymmetric ferromagnetic Weyl semimetal candidate with a Curie temperature of 17.8K, offers a unique platform for exploring the interplay of symmetry breaking and topological electronic structures. Up to now, the Weyl fermion distribution as well as their evolution across the ferromagnetic to paramagnetic phase transition in PrAlSi has not been explored.**
**Here, the presence of Weyl fermions is uncovered in PrAlSi and demonstrates that they can be manipulated through the magnetic phase transition.**
**The ab-initio calculations indicate a shift in the momentum and energy positions of Weyl fermions, alongside an increase in Weyl point numbers due to band splitting. The predicted band splitting and shifting of Weyl fermions are corroborated by the angle-resolved photoemission spectroscopy experiments. Such manipulation of Weyl fermions leads to the appearance of a net chirality charge and a significant modulation in optical conductivity, as proposed by the calculations. The research presents a novel method for adjusting the properties of Weyl semimetals by controlling Weyl fermions through magnetic phase transitions, positioning PrAlSi as a model system.**

## 1. Introduction

In the rapidly developing field of topological materials, Weyl semimetals are distinguished by their topologically nontrivial electronic structures and multifaceted physical phenomena.[1–5] Characterized by linear electron dispersions (Weyl fermions) near nodal points known as Weyl points (WPs), Weyl semimetals feature these points as sources or sinks of Berry curvature in momentum space, each endowed with a specific chirality charge. Moreover, Fermi arc surface states connect a pair of WPs with opposite chirality.[5–9] The realization of Weyl semimetals hinges on the breaking of either inversion symmetry (IS) [5,9–12] or time reversal symmetry (TRS),[7,13–16] giving rise to a diverse array of materials. Weyl semimetals such

---

K. Wang, W. Shi, W. Cao, X. Yang, C. Chen, H. Yang, Y. Chen, Y. Qi, Z. Liu
School of Physical Science and Technology
ShanghaiTech University
Shanghai 201210, China
E-mail: shiwujun@shanghaitech.edu.cn; qiyp@shanghaitech.edu.cn; liuzhk@shanghaitech.edu.cn

K. Wang, W. Cao, X. Yang, C. Chen, H. Yang, Y. Chen, Y. Qi, Z. Liu
ShanghaiTech Laboratory for Topological Physics
ShanghaiTech University
Shanghai 201210, China

W. Shi, Y. Chen
Center for Transformative Science, and Shanghai High Repetition Rate XFEL and Extreme Light Facility (SHINE)
ShanghaiTech University
Shanghai 201210, China

The ORCID identification number(s) for the author(s) of this article can be found under https://doi.org/10.1002/aelm.202500044

**DOI: 10.1002/aelm.202500044**

Z. Lv, M. Ye
Shanghai Institute of Microsystem and Information Technology
Chinese Academy of Sciences
Shanghai 200050, China

C. Peng, Y. Chen
Department of Physics
Clarendon Laboratory
University of Oxford
Parks Road, Oxford OX1 3PU, UK

D. Liu
Department of Physics
Beijing Normal University
Beijing 100875, China

L. Yang
State Key Laboratory of Low Dimensional Quantum Physics
Department of Physics
Tsinghua University
Beijing 100084, China

M. Lyu, P. Sun, E. Liu
Beijing National Laboratory for Condensed Matter Physics
Institute of Physics
Chinese Academy of Sciences
Beijing 100190, China

as TaAs [2,3,5,9–12,17] do not possess IS but maintain TRS, whereas materials like $Co_3Sn_2S_2$ [14,15,18,19] preserve IS while lacking TRS. Different crystal symmetries in Weyl semimetals lead to different distributions of WPs and the chirality charges. The mirror symmetry (MS) and IS related WPs host opposite chirality charge, while other symmetries-related WPs have the same chirality charge.

Weyl fermions and Fermi arcs in Weyl semimetals give rise to a variety of transport and optical phenomena, such as the chiral anomaly in magnetotransport,[20,21] pronounced second-harmonic generation (SHG),[22] and distinctive photocurrent effects.[23] Importantly, these characteristics can be modulated by altering the quantity, arrangement, and nature of WPs and Fermi arcs. To date, numerous strategies for this manipulation have been explored, including the application of external magnetic fields or pressure to transition Dirac semimetals to Weyl semimetals (Figure 1a(i)),[24–26] enhancement of spin-orbit coupling (SOC),[17] and adjustment of WP distribution through external fields or pressure (Figure 1a(ii)),[27–30] as well as the modification of Fermi arcs via surface dosing (Figure 1a(iii)).[31] Despite their effectiveness, these approaches often rely on external interventions like strain, magnetic ordering, element doping, or a vacuum environment, which may limit their practicality in device contexts. In this study, we introduce a new approach that leverages temperature-driven magnetic phase transitions, alongside TRS and MS breaking in noncentrosymmetric magnetic Weyl semimetals (Figure 1a(iv)), exemplified by PrAlSi, to achieve Weyl fermion manipulation without the constraints of previous methods.

Recently, the noncentrosymmetric (thus IS is absent) RAlPn (R = rare earth, Pn = Si, Ge) compounds have been theoretically predicted and experimentally proved to be Weyl semimetals.[32–52] Notably, these materials exhibit diverse magnetic behaviors at low temperatures, ranging from antiferromagnetism in SmAlSi (Neel temperature $T_N \sim 11K$) [38] and CeAlGe ($T_N \sim 5K$),[35,48,53] to complex magnetic transitions in NdAlSi, which shows antiferromagnetic ordering at 7.2 K followed by ferromagnetism at 3.3 K.[46,50] Among these non-centrosymmetric Weyl semimetal candidates, PrAlSi stands out with its ferromagnetic ordering at the highest high Curie temperature (Tc∼17.8 K) and the largest magnetic moment (3.6 $\mu$B/Pr),[39] positioning it as an ideal candidate to explore the interplay between magnetic phase transitions, symmetry breaking, and the manipulation of WPs (Figure 1a(iv)). So far, although there have been studies [52,54] on the effect of magnetism on WPs and Fermi arcs in RAlPn family, there have been reports [52] that the magnetic phase transition causes the surface state of CeAlSi to undergo splitting and the WPs to shift, while there is no change in the electronic structure during the magnetic phase transition in PrAlSi and SmAlSi.[54] However, the existence of the Weyl fermions and their evolution through the ferromagnetic (FM) to paramagnetic (PM) phase transition, has not been systematically established in PrAlSi, especially by angle resolved photoemission spectroscopy (ARPES) measurements.

In this work, we carried out comprehensive ARPES experiments and *ab-initio* calculations to investigate the electronic structure of PrAlSi and its evolution from the PM phase to the FM phase. Our findings reveal a transition from 32 WPs in the PM phase to 56 in the FM phase, driven by band splitting due to the Zeeman effect. This band splitting and the WP shift were directly visualized in ARPES measurement. Furthermore, our theoretical calculation shows that the absence of inversion symmetry (IS) and mirror symmetry (MS) in the FM phase of PrAlSi allows for the manifestation of WPs with opposite chirality charges at different energy levels, introducing a net chirality charge. This unique arrangement of WPs can also introduce novel transport phenomena, such as the emergence of additional peaks in optical conductivity (OC) and large magneto-optic Kerr effect (MOKE) within the FM phase.

## 2. Results And Discussion

### 2.1. Structure, Symmetry, and Magnetic Phase Transition

The PrAlSi has body-centered tetragonal structure in space-group 109 ($I4_1md$) (Figure 1b). The crystal is characterized by a total of eight symmetry operations, which include two symmorphic symmetries (identity operation $E$, and mirror symmetry $m_y$) and six nonsymmorphic symmetries ($C_{2z}$, $C_{4z}^+$, $C_{4z}^-$, $m_x$, $m_{xy}$, and $m_{x\bar{y}}$). All constituent atoms occupy the 4*a* Wyckoff positions, with Pr at (0.5,0.5,0.0762), Si at the origin (0, 0, 0), and Al at (0,0,0.1654). Figure 1c shows the crystal structure and the 3D BZ with the projected (001) surface BZ. Depending on the location in reciprocal space, the combined crystal symmetry and TRS ($\mathcal{T}$) can generate up to sixteen equivalent sites, although this multiplicity reduces to eight for certain positions, such as those within the $k_z = 0$ plane.

Due to the presence of the rare earth element Pr, PrAlSi exhibits ferromagnetic transition below 17.8 K with the magnetic momentum aligning along the *c* axis,[39] as confirmed by our susceptibility measurements (Figure 1d). Across the transition to the FM phase, symmetries such as $m_x$, $m_y$, $m_{xy}$, $m_{x\bar{y}}$, and $\mathcal{T}$ are broken, leaving only the $E$, $C_{2z}$ and $C_{4z}$ symmetries intact. Consequently, in the FM state, the crystal symmetry at most reciprocal-space points is reduced, generating only four equivalent sites, as opposed to the sixteen sites possible in the PM phase for most positions.

### 2.2. Identification and Manipulation of WPs

In our investigation of PrAlSi's electronic structure through first-principles calculations, we discerned 32 Weyl points (WPs) in the paramagnetic (PM) phase, constituting 16 WP pairs as cataloged

M. Ye
Shanghai Synchrotron Radiation Facility
Shanghai Advanced Research Institute
Chinese Academy of Sciences
Shanghai 201204, China

Y. Sun
Institute of Metal Research
Chinese Academy of Sciences
Shenyang 110016, China

Y. Qi
Shanghai Key Laboratory of High-resolution Electron Microscopy
ShanghaiTech University
Shanghai 201210, China

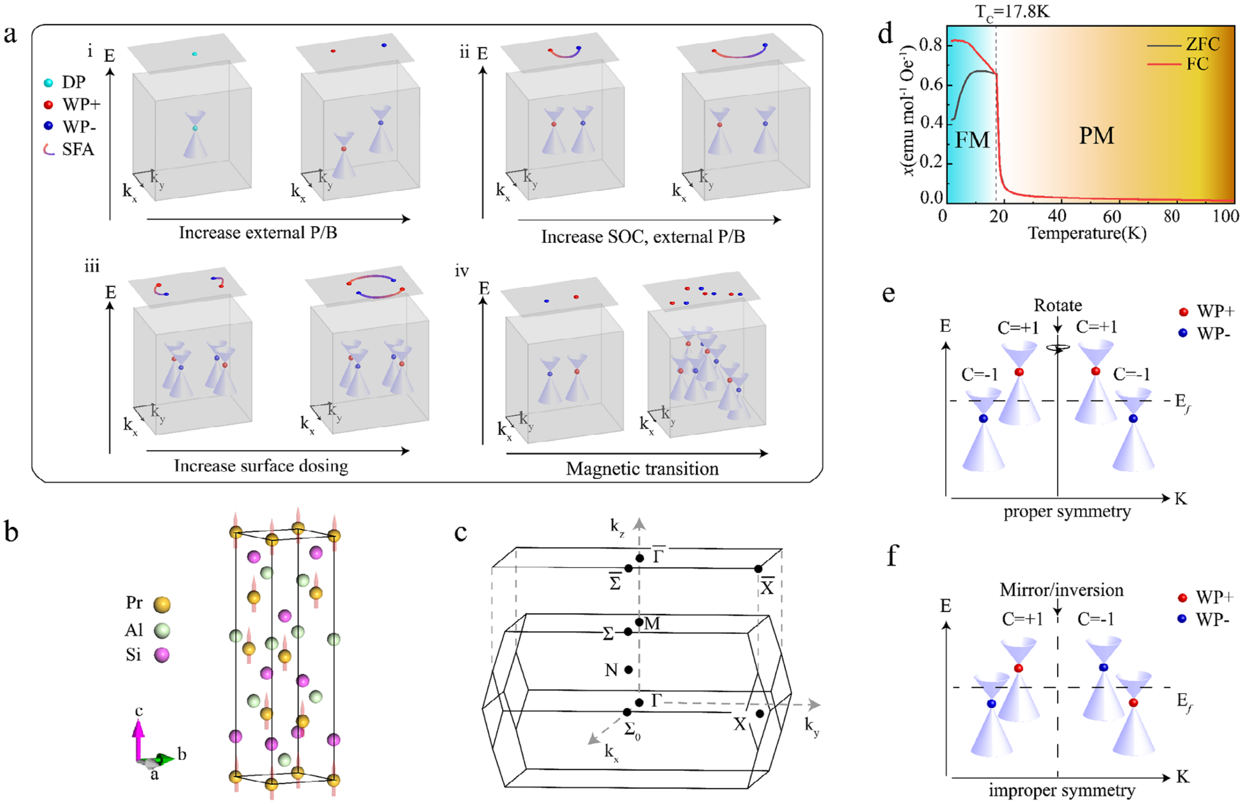

**Figure 1.** Manipulations of Weyl Fermions (WPs) and properties of PrAlSi. a) Possible scenarios of WPs and surface Fermi Arcs (SFA) manipulations. The red/blue dots represent WPs with opposite chirality charge. (i) Break degenerate Dirac point (DP) into WPs by external pressure (P) or magnetic field (B) through breaking IS or TRS. (ii) Enlarge the WPs' separation by increasing the SOC strength or increasing external P/B. (iii) Change the connection of FAs by surface dosing. (iv) Manipulate and proliferate the WPs through TRS breaking magnetic transitions. b) Crystal structure of PrAlSi. The magnetic order in FM phase is along the (001) direction, as indicated by the red arrows. c) Illustration of the 3D BZ of PrAlSi, and the corresponding (001) surface BZ. d) Zero-field cooled (ZFC, black curve) and field-cooled (FC, red curve, with magnetic field applied perpendicular to the *c* axis) magnetic susceptibility ($\chi$) as functions of temperature. e,f) Schematics of the proper (rotation) and improper (mirror and inversion) operation related WPs. $E_f$: Fermi level. The net chirality charge below $E_f$ is 2 in (e) and 0 in (f).

in **Table 1**. The momentum distribution of these WPs within the first BZ is illustrated from both top (001) and side (010) views in Figure S1 (Supporting Information). These WPs are categorized into three distinct types of inequivalent pairs: $W_1$, $W_2$, and $W_3$. Specifically, 8 $W_1$ pairs are situated in the $k_z = \pm 0.287$ Å$^{-1}$ plane, while both $W_2$ and $W_3$ types, comprising 4 pairs each, reside in the $k_z = 0$ plane (Figure S1, Supporting Information). Each pair consists of WPs of opposite chirality, denoted as $W_1^+/W_1^-$, $W_2^+/W_2^-$ and $W_3^+/W_3^-$ with "+" and "−" indicating positive and negative chirality charges, respectively. These pairs are symmetrically related by different mirror planes ($m_x$, $m_y$, $m_{xy}$, $m_{x\bar{y}}$), and intriguingly, they align at identical energy levels, as shown in Figure 1f, ensuring a net chirality charge of zero below the Fermi level. However, by deliberately disrupting the MS by introducing magnetism, it becomes possible to shift the energy levels of WPs with opposing charges, as depicted in Figure 1e. Such manipulation enables the induction of a net chirality charge beneath the Fermi level, opening avenues for novel topological phenomena.

As PrAlSi transitions to the FM phase at lower temperatures, MSs and TRS are disrupted, primarily due to magnetism from the Pr 4*f* electrons. This leads to band splitting in the low-energy bands near the Fermi level, predominantly composed of Al and Si orbitals. This phenomenon, as evidenced by ARPES measurements, subsequently influences the manipulation of the WPs in the following aspects (locations listed in Table 1 and plotted in Figure S1, Supporting Information): (1) The emergence of additional WPs due to magnetism-induced band splitting, resulting in three more WP pairs near each $W_3$ pair and a total of 56 WPs in the FM phase. (2) Increment of momentum separation of existing WPs within the same group, driven by band splitting. Notably, $W_2$ and $W_3$ pairs experience significant shifts in momentum space. (3) In the FM phase, broken MSs lead to WPs of opposite chirality residing at different energy levels, enabling the adjustment of the Fermi level to achieve a net chirality charge (see detailed discussion in Supporting Information). These manipulations underscore the intricate interplay between magnetic transitions and topological properties in PrAlSi.

### 2.3. Calculations of the Electronic Structure

To elucidate the mechanisms behind the manipulation of WPs, we conducted electronic band structure calculations for PrAlSi along high-symmetry directions, considering both the

**Table 1.** The designated groups of symmetry related WPs in PrAlSi. For each group, we list the number of WPs, and the momentum position and energy of one WPs.

| | PM Phase | | | FM Phase | | |
|---|---|---|---|---|---|---|
| WPs | Multiplicity | Coordinates[1/Å] | E-$E_f$ [meV] | Multiplicity | Coordinates[1/Å] | E-$E_f$ [meV] |
| $W_1^+$ | 8 | (0.01824, 0.37241, 0.28742) | 27.7 | 4 | (0.03767, 0.39084, 0.28062) | 28.9 |
| | | | | 4 | (0.05072, 0.35791, -0.28020) | 3.3 |
| $W_1^-$ | 8 | (0.37241, 0.01824, 0.28742) | 27.7 | 4 | (0.35774, 0.05037, 0.28062) | 3.6 |
| | | | | 4 | (0.39119, 0.03721, -0.28072) | 29.0 |
| $W_2^+$ | 4 | (0.74230, 0.00344, 0.0) | 61.9 | 4 | (0.76379, 0.01066, -0.03426) | 57.1 |
| $W_2^-$ | 4 | (0.00344, 0.74230, 0.0) | 61.9 | 4 | (0.01052, 0.76391, 0.03454) | 57.4 |
| $W_3^+$ | 4 | (0.26440, 0.34227, 0.0) | 91.6 | 4 | (0.26423, 0.42128, -0.00069) | 85.5 |
| | | | | 4 | (0.24377, 0.32376, -0.00361) | 54.1 |
| | | | | 4 | (0.30600, 0.25187, 0.05471) | 24.8 |
| | | | | 4 | (0.30602, 0.24967, -0.05556) | 29.3 |
| $W_3^-$ | 4 | (0.34227, 0.26440, 0.0) | 91.6 | 4 | (0.42145, 0.26411, 0.00068) | 85.6 |
| | | | | 4 | (0.32393, 0.24366, 0.00351) | 54.4 |
| | | | | 4 | (0.25192, 0.30588, -0.05469) | 24.7 |
| | | | | 4 | (0.24972, 0.30596, 0.05562) | 29.3 |

presence and absence of SOC in the PM and FM phases (refer to Figure S2, Supporting Information). In the PM phase, spin-up and spin-down bands remain degenerate without SOC, while SOC induces splitting except at time-reversal invariant momentum (TRIM) points and along the $\Gamma - M$ line. At TRIM points, the TRS preserves the two-fold band degeneracy, whereas along the $\Gamma - M$ line, the $C_{4v}$ symmetry ensures it (Figure S2a, Supporting Information). Transitioning to the FM phase, magnetism disrupts TRS and MSs, leading to the splitting of spin-degenerate bands at TRIM points and along the $\Gamma - M$ line into distinct spin-up and spin-down bands, with SOC further widening this gap (Figure S2b, Supporting Information).

The band splitting fosters the emergence and relocation of WPs, as detailed previously. Our calculations also extend to the Fermi surface for PrAlSi in both phases (Figure S2c,d, Supporting Information). In the PM phase, electron and hole pockets respect various symmetries, including $C_{2z}$, $C_{4z}^+$, $C_{4z}^-$, $m_x$, $m_{xy}$, and $m_{x\bar{y}}$, whereas in the FM phase, only $C_{2z}$, $C_{4z}^+$ and $C_{4z}^-$ Symmetries persist, with all pockets expanding in size, indicative of increased band crossings at the Fermi level.

Further analysis of the electronic band structures on the PrAlSi (001) surface, employing a slab model, reveals that the bulk states undergo splitting in the FM phase (Figure 2d–f for the PM phase and Figure 2j–l for the FM phase). We note the calculated surface states exhibit $C_2$ symmetry, diverging from the $C_4$ symmetry of bulk states. This discrepancy arises from the disruption of $C_{4z}$ symmetry due to the absence of translational symmetry along the *c*-axis upon cleaving the (001) surface.

### 2.4. ARPES Measurement of PrAlSi

Our ARPES experiments on the (001) surface of PrAlSi were conducted in both PM and FM phases, as shown in Figure 2. The measurements were conducted at photon energy of 94 eV, corresponding to $k_z = 5.182$ Å$^{-1}$ ($\frac{24\pi}{c}$), (see more $k_z$ measurement in Figure S5, Supporting Information). Constant energy contours (Figure 2a,g) and dispersions along various high symmetry directions (Figure 2b,c,h,i) highlight the presence of distinct bulk and surface band dispersions, closely matching our slab model predictions (Figure 2d–f,j–l, also see Figure S11, Supporting Information), except for the surface states in FM state, which may be due to the weak coupling between f-electrons and the surface states or the surface reconstruction and contamination. The observation of relatively broad spectral weight distribution of bulk states indicates significant $k_z$ broadening (Figure 2b,c,h,i, also see Figures S5 and S9, Supporting Information). Our experimental results validate the existence of Weyl fermions, while the measured surface states exhibit $C_2$ symmetry (Figure 2a,d,g,j), albeit slightly shifted in energy due to potential surface doping after cleavage. Although the electronic structure evolution across the FM to PM phase transition could not be clearly identified by the Fermi surface mapping in Figure 2a,g, the temperature-dependent ARPES measurements along the $\bar{X} - \bar{\Gamma} - \bar{X}$ direction illustrate the band splitting and Weyl fermion ($W_3$) evolution across the FM to PM phase transition (Figure **3**).

Temperature-dependent ARPES measurements along the $\bar{X} - \bar{\Gamma} - \bar{X}$ direction illustrate the band splitting and Weyl fermion ($W_3$) evolution across the FM to PM phase transition (Figure 3). Figure 3a presents a set of spectra taken at consecutive temperatures, where the band splitting within the bulk valence band (BVB) in the FM state is observed, most prominent for the uppermost BVB near $\bar{\Gamma}$. This bulk band splitting is most pronounced at 8.9 K, decreases with temperature and disappears above Tc (Figure 3d, also see the cooled down data in Figure S7, Supporting Information). The magnitude of the splitting ($\Delta_{\text{gap}}$) follows a mean-field-like temperature dependence $\Delta \sim \sqrt{1 - \frac{T}{T_c}}$, suggesting a direct correlation with magnetization (Figure 3e). The band splitting along $\bar{\Sigma} - \bar{\Gamma} - \bar{\Sigma}$ and $\bar{X} - \bar{\Gamma} - \bar{X}$ with varying photon energies is documented in the supplemental materials (Figure S6a–d, Supporting Information). These observations

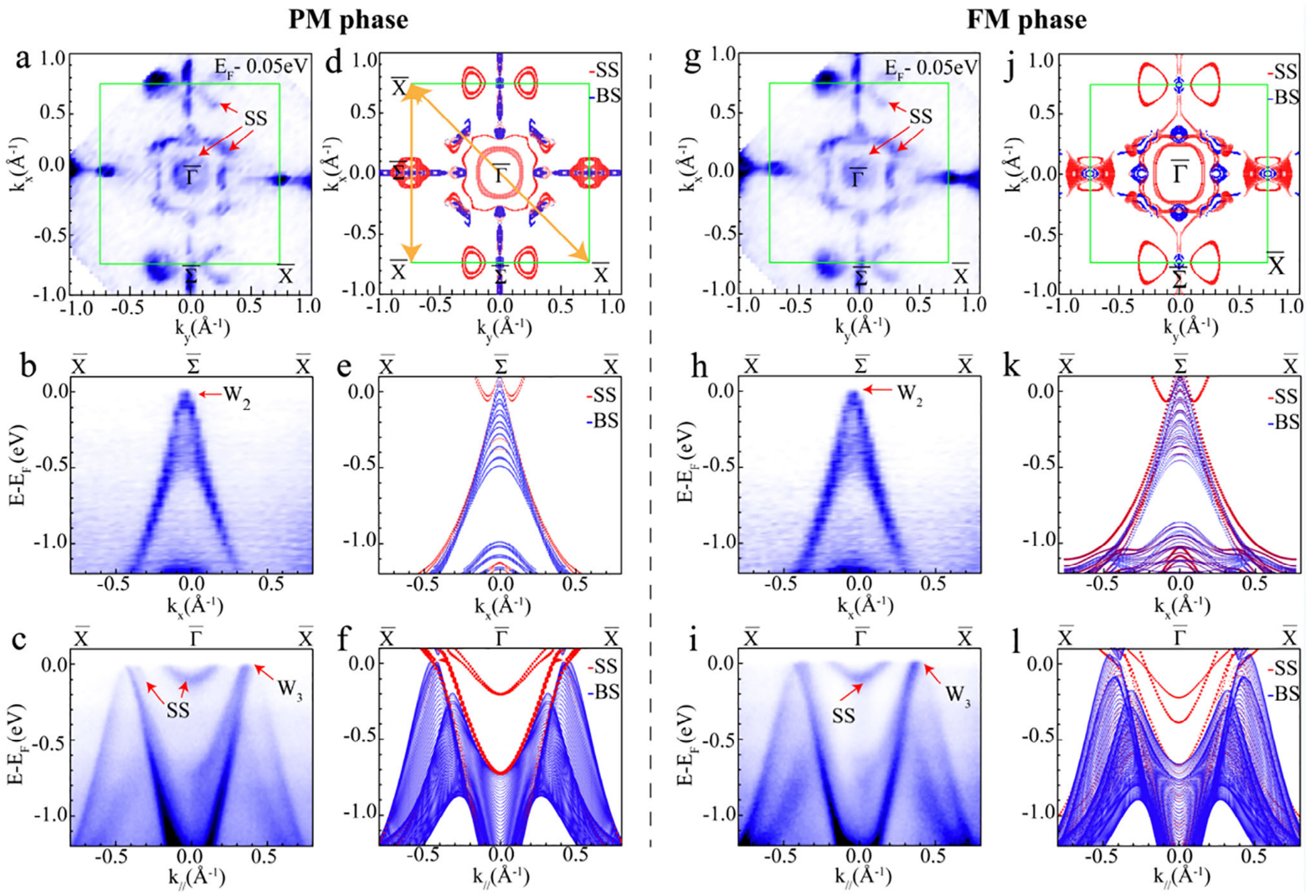

**Figure 2.** Electronic band structure of PrAlSi. a–f) The ARPES and slab calculation results of PrAlSi in the PM phase. (a) Intensity plot of the ARPES constant energy contour near $E_F$, integrated from $E_F$ to 0.05 eV below. (b,c) Intensity plot of the band dispersions along the $\bar{X}-\bar{\Sigma}-\bar{X}$ (b) and $\bar{X}-\bar{\Gamma}-\bar{X}$ (c) directions as indicated by the arrows in (d). $W_2$ and $W_3$ label the positions of the WPs. (d–f) Corresponding slab calculation results. SS: surface electronic state. BS: bulk electronic state. g–l) The same as (a–f) but in the FM phase.

corroborate that band splitting occurs at TRIM points (see schematic in Figure S6e, Supporting Information), as a result of TRS breaking, aligning with theoretical predictions.

Moreover, the ARPES data in the FM phase provide direct evidence of Weyl fermions' displacement associated with the band splitting. Detailed examination of the band dispersions near the Fermi level (Figure 3b,c) revealed the emergence of additional band crossings in the FM phase, contrasted with the PM phase findings (indicated by the green and red arrows in Figure 3b). This observation, aligned with slab model predictions, was substantiated by momentum distribution curve analysis (Figure 3c,f,h), which showed the merging of two bulk valence band peaks into a single peak across the FM to PM phase transition (Figure 3f,h). A discernible band splitting was observed at low temperatures ($\Delta_{\mathrm{split}} \sim 0.037$ Å$^{-1}$ at 8.9K), which disappears above Tc, suggesting a band splitting induced Weyl fermion ($W_3$) shift. The momentum splitting is accompanied by a shift in the energy at the band top ($E_{\mathrm{top}}$), as highlighted by the green arrow on the far left in Figure 3b,c. This observation is corroborated by the analysis of the energy distribution curves (shown in Figure 3g,h), which reveal that $E_{\mathrm{top}}$ undergoes a shift of ≈25 meV toward the adjacent band across the transition from FM to PM states. Similar band shift in energy and momentum could also be observed in $W_1$ Weyl fermions (see Figure S8, Supporting Information). These results underscore the feasibility of manipulating Weyl fermions through band splitting and shifting, facilitated by magnetic phase transitions in PrAlSi.

### 2.5. Optical Conductivity and Magneto-Optical Kerr Effect

The transition from the PM to the FM phase, accompanied by the breaking of TRS and MS, sets the stage for the emergence of novel transport and optical phenomena, such as SHG, distinctive OC, and magneto-optical Kerr effect (MOKE) profiles. The OC, a critical parameter for probing allowed interband optical transitions, was rigorously analyzed in this study (Figure 4a). The OC was computed using the Kubo formula:[55,56]

$$\sigma_{\alpha\beta}(\omega) = -\frac{ie^2}{\hbar}\sum_{n,n'}\int\frac{d^3\mathbf{k}}{(2\pi)^3}\frac{f(n',\mathbf{k})-f(n,\mathbf{k})}{\varepsilon(n,\mathbf{k})-\varepsilon(n',\mathbf{k})} \times\frac{M^{\alpha}_{nn'}(\mathbf{k})\,M^{\beta}_{n'n}(\mathbf{k})}{\hbar\omega+\varepsilon(n',\mathbf{k})-\varepsilon(n,\mathbf{k})+i\eta} \tag{1}$$

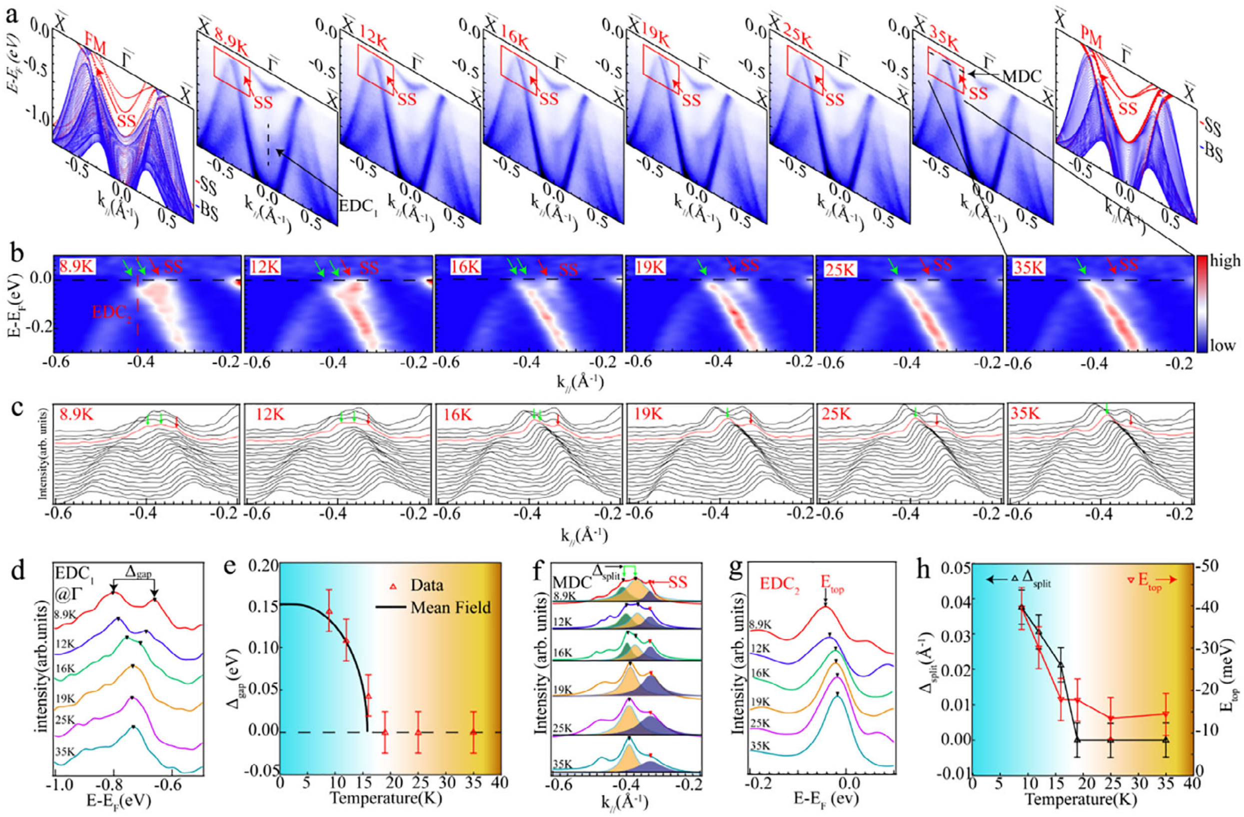

**Figure 3.** Temperature evolution of the energy dispersion along $\bar{X}-\bar{\Gamma}-\bar{X}$ direction. a) Intensity plots of the band dispersion along $\bar{X}-\bar{\Gamma}-\bar{X}$ direction at different temperatures. The calculated dispersions in the FM (PM) phase are labeled on the most the left (right) panel. SS: surface electronic state. b) The zoomed-in plots of the corresponding red rectangular boxes in (a). The green and red arrows label the bulk and surface bands, respectively. c) The stacked line plots of the MDC of (b). d) Plot of the EDCs at the $\bar{\Gamma}$ point at various temperatures. e) Plot of the energy gap between two peaks marked by black arrows in (d) as a function of temperature. The black curve represents the mean-field fitting results. f) Plot of the MDCs near $E_F$ (indicated by the black dashed line in the 35K data in (a) and red MDC in (c)) at different temperatures. The shaded peaks indicated the Lorentzian fitting results of the bulk (labelled by the green arrows) and surface (labelled by the red arrows) peaks, respectively. g) Plot of the EDCs along the red dashed line (near the band top) in (b) at different temperatures. h) Plot of the momentum splitting ($\Delta_{split}$) of the bulk peaks marked by green arrows in (f) and band top energy ($E_{top}$) marked in (g) as a function of temperature.

where $\alpha,\ \beta = x,\ y,\ z,\ f = 1/[1+e^{(\varepsilon-\mu)/k_b T}]$ is the Fermi-Dirac distribution, $\mu$ is the chemical potential, $k_b$ is the Boltzmann constant, T is the temperature, $M^{\alpha}_{nn'}(\boldsymbol{k}) = \langle n,\boldsymbol{k}|\hbar v_\alpha|n',\boldsymbol{k}\rangle = \langle\frac{\partial(n,\boldsymbol{k})}{\partial \boldsymbol{k}_\alpha}|n',\boldsymbol{k}\rangle\,[\varepsilon(n,\boldsymbol{k})-\varepsilon(n',\boldsymbol{k})]$, $v_\alpha = \frac{1}{\hbar}\frac{\partial H(\boldsymbol{k})}{\partial \boldsymbol{k}_\alpha}$ is the velocity operator.

In the PM phase, TRS mandates that all off-diagonal OC tensor components vanish ($\sigma_{xy} = \sigma_{xz} = \sigma_{yx} = \sigma_{yz} = \sigma_{zx} = \sigma_{zy} = 0$), and the $C_{4z}$ crystal symmetry forces $\sigma_{xx} = \sigma_{yy}$. Conversely, in the FM phase, the magnetic moments along the $z$-axis disrupts TRS, eliminating $\sigma_{xz}$, $\sigma_{yz}$, $\sigma_{zx}$, and $\sigma_{zy}$ while enabling a nonzero $\sigma_{xy}$ and $\sigma_{yx}$ (anomalous Hall-like conductivity).

From the OC tensor, the complex Kerr angle $\phi_K = \theta_K + i\epsilon_K$ of MOKE can be given by[57]

$$\phi_K(\omega) = \frac{-\sigma_{xy}}{\sigma_{xx}\sqrt{1+i\,(4\pi/\omega)\,\sigma_{xx}}} \tag{2}$$

The calculated imaginary part OC in both PM ($\sigma_{xx}$ and $\sigma_{zz}$) and FM ($\sigma_{xy}$, $\sigma_{xx}$ and $\sigma_{zz}$) phase, and imaginary part Kerr angle are displayed in Figure 4c–h, and the included bands are shown in Figure 4a,b. The chemical potential ($\mu$) was fine-tuned within a ± 0.1 eV range around the calculated Fermi level ($E_f$). The results underscore the anisotropy in OC, aligning with the crystal's symmetrical properties. Notably, the FM phase showcases additional OC peaks absent in the PM phase, attributed to photon-induced interband transitions among the four bands near the Fermi level. Among these, the anomalous Hall-like OC ($\sigma_{xy}$) and Kerr angle induced by the magnetic ordering in the FM phase, stands out as a pivotal finding (Figure 4f). The largest Kerr angle is ≈0.2 degrees at small photon energies. This novel OC/MOKE behavior, particularly the photon-induced anomalous Hall conductivity, is anticipated to be experimentally observable by Terahertz spectroscopy, offering new insights into the optical properties of magnetic Weyl semimetals.

## 3. Conclusion

In conclusion, we systematically investigated the electronic structure of PrAlSi and confirmed it to be a Weyl semimetal in both the PM and FM phases. Using the first-principles calculation and ARPES experiments, we uncover the manipulation of Weyl fermions through magnetic phase transition, including the

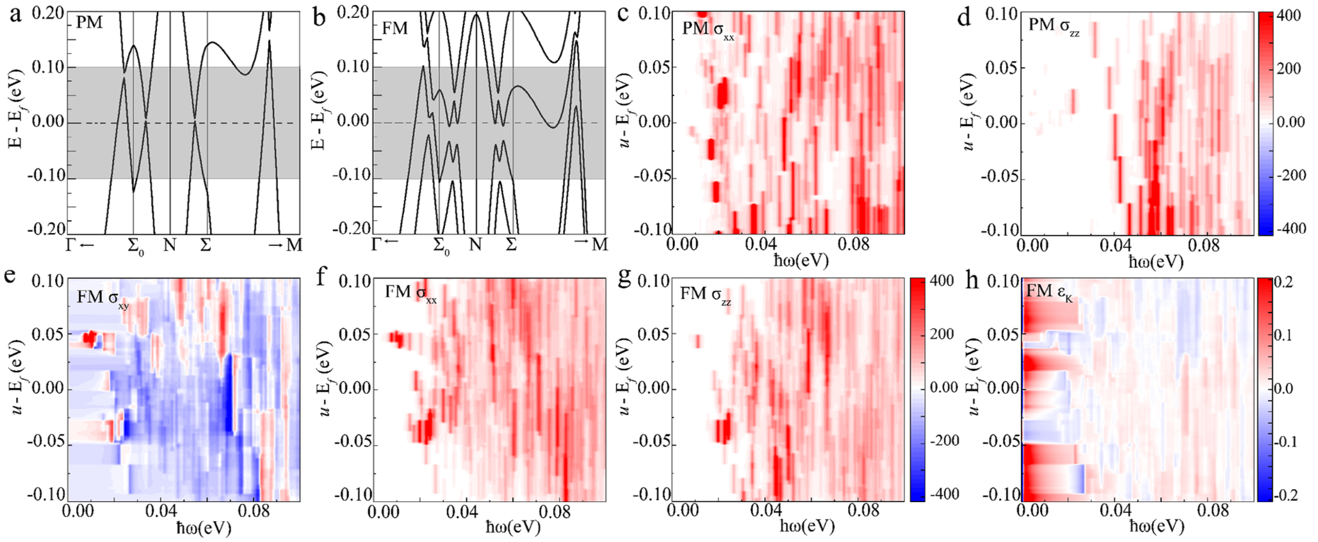

**Figure 4.** The calculated optical conductivity and Kerr angles of PrAlSi. a,b) The selected bands to calculate OCs and Kerr angles in the PM and FM phases, respectively. c–d) The calculated imaginary part of OC $\sigma_{xx}$, and $\sigma_{zz}$ as a function of incident photon energy and the adjusted chemical potential. e–g) The calculated imaginary part of OC $\sigma_{xy}$, $\sigma_{xx}$, and $\sigma_{zz}$ as a function of incident photon energy and the adjusted chemical potential. h) The calculated imaginary part of the Kerr angle $\epsilon_K$. as a function of incident photon energy and the adjusted chemical potential. $\mu$: adjusted chemical potential. $E_f$: calculated Fermi level.

number of WPs and the WP distribution in momentum and energy space. Specifically, this special distribution of WPs in the FM phase leads to net chirality charge beneath the Fermi level, and the emergence of new physical properties such as anomalous Hall-like OC and large Kerr angle. Our results provide strong evidence for the influence of magnetism and topology in Weyl semimetals with both IS and TRS broken and provide new routes to manipulate Weyl fermions for spintronics and optoelectronics applications.

## 4. Experimental Section

*Crystal Growth*: Single crystals of PrAlSi were synthesized via the self-flux method,[33,39] employing high-purity Pr, Si, and Al in a 1:1:10 molar ratio. The mixture was placed in an alumina crucible within an argon atmosphere glove box, then vacuum-sealed in a quartz tube. The assembly was heated to 1100 °C over 24 h, maintained at this temperature for 12 h to ensure complete melting, and then gradually cooled to 750 °C at a rate of 2 °C $h^{-1}$. Excess Al was removed post-cooling using a centrifuge.

*ARPES Experiment*: ARPES measurements were performed at BL 10.0.1, BL 7.0.2, and BL 4.0.3 of the Advanced Light Source, BL 5-2 of the Stanford Synchrotron Radiation Light Source, alongside a helium lamp-equipped setup at Shanghaitech University. Measurements spanned temperatures from 5K to 250K under a vacuum below $5.0 \times 10^{-11}$ Torr. The setups offered an angular resolution of 0.1° and energy resolutions of better than 10 and 5 meV for photon energies of 100 and 21 eV, respectively.

*First-Principles Calculations*: The first-principles calculations were performed using the Vienna ab initio Simulation Package (VASP).[58] The interactions between the valence electrons and ion cores were described by the projector augmented wave method,[59,60] and the exchange-correlation potential was formulated by the generalized gradient approximation with the Perdew-Burke-Ernzerhof (PBE) scheme.[61] The $\Gamma$-centered $20 \times 20 \times 20$ k-points were used for the first Brillouin-zone (BZ) sampling. The kinetic energy cutoff was set to 500 eV. First, the crystal structure was fully relaxed until the force was less than 0.02 eV Å$^{-1}$, and the relaxed lattice constants of conventional cell were $a = b = 4.255$ Å, and $c = 14.636$ Å, which was close to the experiment results ($a = b = 4.23$ Å, and $c = 14.55$ Å). For the FM phase, the Pr 4*f* electrons were treated as the valence electrons, while for the PM phase, the Pr 4*f* electrons were treated as the core electrons. For the FM phase calculations, a Hubbard U = 6 eV was applied on the Pr 4*f* electrons to push the 4*f* band away from the Fermi level, which was the origin of magnetic momentum. To calculate the surface states, a slab model of 10 conventional cells separated by 20 Å vacuum was employed. The SOC was included in calculations. For the OC calculations, a dense $60 \times 60 \times 60$ k-points grid was employed. The chemical potential ($\mu$) was set ±0.1 eV around the calculated Fermi level ($E_f$), and a 0 to 0.1 eV range of photon energy was considered.

## Supporting Information

Supporting Information is available from the Wiley Online Library or from the author.

## Acknowledgements

K.P.W, W.J.S., and W.Z.C. contributed equally to this work. Z. K. Liu acknowledges the support from the National Natural Science Foundation of China (92365204, 12274298) and the National Key R&D program of China (Grant No. 2022YFA1604400/03). W. J. Shi acknowledges the support from Science and Technology Commission of Shanghai Municipality (STCSM) (Grant No. 22ZR1441800), and HPC Platform of ShanghaiTech University. Y. P. Qi acknowledges the support from the National Natural Science Foundation of China (Grant No. 52272265) and the National Key R&D Program of China (Grant No. 2023YFA1607400).

## Conflict of Interest

The authors declare no conflict of interest.

## Data Availability Statement

The data that support the findings of this study are available from the corresponding author upon reasonable request.

## Keywords

ab-initio calculations, angle-resolved photoemission spectroscopy, electronic structure, magnetic transition, topological weyl semimetal

Received: January 17, 2025
Published online:

[1] H. Weyl, *Z. Phys.* **1929**, *56*, 330.
[2] B. Q. Lv, N. Xu, H. M. Weng, J. Z. Ma, P. Richard, X. C. Huang, L. X. Zhao, G. F. Chen, C. E. Matt, F. Bisti, V. N. Strocov, J. Mesot, Z. Fang, X. Dai, T. Qian, M. Shi, H. Ding, *Nat. Phys.* **2015**, *11*, 724.
[3] S. Y. Xu, N. Alidoust, I. Belopolski, Z. Yuan, G. Bian, T. R. Chang, H. Zheng, V. N. Strocov, D. S. Sanchez, G. Chang, C. L. Zhang, D. X. Mou, Y. Wu, L. Huang, C.-C. Lee, S.-M. Huang, B. Wang, A. Bansil, H.-T. Jeng, T. Neupert, A. Kaminski, H. Lin, S. Jia, M. Z. Hasan, *Nat. Phys.* **2015**, *11*, 748.
[4] B. Yan, C. Felser, *Annu. Rev. Condens. Matter Phys.* **2017**, *8*, 337.
[5] B. Q. Lv, H. M. Weng, B. B. Fu, X. P. Wang, H. Miao, J. Ma, P. Richard, X. C. Huang, L. X. Zhao, G. F. Chen, Z. Fang, X. Dai, T. Qian, H. Ding, *Phys. Rev. X* **2015**, *5*, 031013.
[6] D. Takane, Z. Wang, S. Souma, K. Nakayama, T. Nakamura, H. Oinuma, Y. Nakata, H. Iwasawa, C. Cacho, T. Kim, K. Horiba, H. Kumigashira, T. Takahashi, Y. Ando, T. Sato, *Phys. Rev. Lett.* **2019**, *122*, 076402.
[7] X. Wan, A. M. Turner, A. Vishwanath, S. Y. Savrasov, *Phys. Rev. B* **2011**, *83*, 205101.
[8] Z. Rao, H. Li, T. Zhang, S. Tian, C. Li, B. Fu, C. Tang, L. Wang, Z. Li, W. Fan, J. Li, Y. Huang, Z. Liu, Y. Long, C. Fang, H. Weng, Y. Shi, H. Lei, Y. Sun, T. Qian, H. Ding, *Nature* **2019**, *567*, 496.
[9] S. Y. Xu, I. Belopolski, N. Alidoust, M. Neupane, G. Bian, C. Zhang, R. Sankar, G. Chang, Z. Yuan, C.-C. Lee, S.-M. Huang, H. Zheng, J. Ma, D. S. Sanchez, B. Wang, A. Bansil, F. Chou, P. P. Shibayev, H. Lin, S. Jia, M. Z. Hasan, *Science* **2015**, *349*, 613.
[10] H. Weng, C. Fang, Z. Fang, B. A. Bernevig, X. Dai, *Phys. Rev. X* **2015**, *5*, 011029.
[11] L. X. Yang, Z. K. Liu, Y. Sun, H. Peng, H. F. Yang, T. Zhang, B. Zhou, Y. Zhang, Y. F. Guo, M. Rahn, D. Prabhakaran, Z. Hussain, S.-K. Mo, C. Felser, B. Yan, Y. L. Chen, *Nat. Phys.* **2015**, *11*, 728.
[12] S. M. Huang, S. Y. Xu, I. Belopolski, C. C. Lee, G. Chang, B. Wang, N. Alidoust, G. Bian, M. Neupane, C. Zhang, S. Jia, A. Bansil, H. Lin, M. Z. Hasan, *Nat. Commun.* **2015**, *6*, 7373.
[13] A. Sakai, Y. P. Mizuta, A. A. Nugroho, R. Sihombing, T. Koretsune, M.-T. Suzuki, N. Takemori, R. Ishii, D. Nishio-Hamane, R. Arita, P. Goswami, S. Nakatsuji, *Nat. Phys.* **2018**, *14*, 1119.
[14] D. F. Liu, A. J. Liang, E. K. Liu, Q. N. Xu, Y. W. Li, C. Chen, D. Pei, W. J. Shi, S. K. Mo, P. Dudin, T. Kim, C. Cacho, G. Li, Y. Sun, L. X. Yang, Z. K. Liu, S. S. P. Parkin, Y. L. Chen, *Science* **2019**, *365*, 1282.
[15] E. Liu, Y. Sun, N. Kumar, L. Muechler, A. Sun, L. Jiao, S.-Y. Yang, D. Liu, A. Liang, Q. Xu, J. Kroder, V. Süß, H. Borrman, C. Sheknar, Z. Wang, C. Xi, W. Wang, W. Schnelle, S. Wirth, Y. Chen, S. T. B. Goennenwein, C. Felser, *Nat. Phys.* **2018**, *14*, 1125.
[16] I. Belopolski, K. Manna, D. S. Sanchez, G. Chang, B. Ernst, J. Yin, S. S. Zhang, T. Cochran, N. Shumiya, H. Zheng, B. Singh, G. Bian, D. Multer, M. Litskevich, X. Zhou, S.-M. Huang, B. Wang, T.-R. Chang, S.-Y. Xu, A. Bansil, C. Felser, H. Lin, M. Z. Hasan, *Science* **2019**, *365*, 1278.
[17] Z. K. Liu, L. X. Yang, Y. Sun, T. Zhang, H. Peng, H. F. Yang, C. Chen, Y. Zhang, Y. F. Guo, D. Prabhakaran, M. Schimidt, Z. Hussain, S.-K. Mo, C. Felser, B. Yan, Y. L. Chen, *Nat. Mater.* **2016**, *15*, 27.
[18] Q. Wang, Y. Xu, R. Lou, Z. Liu, M. Li, Y. Huang, D. Shen, H. Weng, S. Wang, H. Lei, *Nat. Commun.* **2018**, *9*, 3681.
[19] N. Morali, R. Batabyal, P. K. Nag, E. Liu, Q. Xu, Y. Sun, B. Yan, C. Felser, N. Avraham, H. Beidenkopf, *Science* **2019**, *365*, 1286.
[20] D. T. Son, B. Z. Spivak, *Phys. Rev. B* **2013**, *88*, 104412.
[21] A. Lucas, R. A. Davison, S. Sachdev, *Proc. Natl. Acad. Sci. USA* **2016**, *113*, 9463.
[22] T. Morimoto, S. Zhong, J. Orenstein, J. E. Moore, *Phys. Rev. B* **2016**, *94*, 245121.
[23] H. Weng, *Nat. Mater.* **2019**, *18*, 428.
[24] B. Xie, H. Liu, H. Cheng, Z. Liu, J. Tian, S. Chen, *Light: Sci. Appl.* **2020**, *9*, 201.
[25] B. C. Park, T. Ha, K. I. Sim, T. S. Jung, J. H. Kim, Y. Kim, Y. H. Lee, T. T. Kim, S. W. Kim, *Sci. Adv.* **2022**, *8*, abq2479.
[26] B. Cheng, T. Schumann, S. Stemmer, N. P. Armitage, *Sci. Adv.* **2021**, *7*, abg0914.
[27] Z. Ren, H. Li, S. Sharma, D. Bhattarai, H. Zhao, B. Rachmilowitz, F. Bahrami, F. Tafti, S. Fang, M. P. Ghimire, Z. Wang, I. Zeljkovic, *npj Quantum Mater* **2022**, *7*, 109.
[28] Z. Song, J. Zhao, Z. Fang, X. Dai, *Phys. Rev. B* **2016**, *94*, 214306.
[29] J. Yuan, X. Shi, H. Su, X. Zhang, X. Wang, N. Yu, Z. Zou, W. Zhao, J. Liu, Y. Guo, *Phys. Rev. B* **2022**, *106*, 054411.
[30] S. Dissanayake, C. Duan, J. Yang, J. Liu, M. Matsuda, C. Yue, J. A. Schneeloch, J. C. Y. Teo, D. Louca, *npj Quantum Mater.* **2019**, *4*, 45.
[31] H. F. Yang, L. X. Yang, Z. K. Liu, Y. Sun, C. Chen, H. Peng, M. Schmidt, D. Prabhakaran, B. A. Bernevig, C. Felser, B. H. Yan, Y. L. Chen, *Nat. Commun.* **2019**, *10*, 3478.
[32] G. Chang, B. Singh, S.-Y. Xu, G. Bian, S.-M. Huang, C.-H. Hsu, I. Belopolski, N. Alidoust, D. S. Sanchez, H. Zheng, H. Lu, X. Zhang, Y Bian, T.-R. Chang, H.-T. Jeng, A. Bansil, H. Hsu, S. Jia, T. Neupert, H. Lin, M. Z. Hasan, *Phys. Rev. B* **2018**, *97*, 041104.
[33] W. Cao, N. Zhao, C. Pei, Q. Wang, Q. Zhang, T. Ying, Y. Zhao, L. Gao, C. Li, N. Yu, L. Gu, Y. Chen, K. Liu, Y. Qi, *Phys. Rev. B* **2022**, *105*, 174502.
[34] B. Meng, H. Wu, Y. Qiu, C. Wang, Y. Liu, Z. Xia, S. Yuan, H. Chang, Z. Tian, *APL Mater.* **2019**, *7*, 051110.
[35] P. Puphal, C. Mielke, N. Kumar, Y. Soh, T. Shang, M. Medarde, J. S. White, E. Pomjakushina, *Phys. Rev. Mater.* **2019**, *3*, 024204.
[36] H. Hodovanets, C. J. Eckberg, P. Y. Zavalij, H. Kim, W. C. Lin, M. Zic, D. J. Campbell, J. S. Higgins, J. Paglione, *Phys. Rev. B* **2018**, *98*, 245132.
[37] L. Wu, S. Chi, H. Zuo, G. Xu, L. Zhao, Y. Luo, Z. Zhu, *npj Quantum Mater.* **2023**, *8*, 4.
[38] L. Xu, H. Niu, Y. Bai, H. Zhu, S. Yuan, X. He, Y. Han, L. Zhao, Y. Yang, Z. Xia, et al., *J. Phys.: Condens. Matter* **2022**, *34*, 485701.
[39] M. Lyu, J. Xiang, Z. Mi, H. Zhao, Z. Wang, E. Liu, G. Chen, Z. Ren, G. Li, P. Sun, *Phys. Rev. B* **2020**, *102*, 085143.
[40] D. S. Sanchez, G. Chang, I. Belopolski, H. Lu, J.-X. Yin, N. Alidoust, X. Xu, T. A. Cochran, X. Zhang, Y. Bian, S. S. Zhang, Y.-Y. Liu, J. Ma, G. Bian, H. Lin, S.-Y. Xu, S. Jia, M. Z. Hasan, *Nat. Commun.* **2020**, *11*, 3356.
[41] H. Y. Yang, B. Singh, J. Gaudet, B. Lu, C.-Y. Huang, W.-C. Chiu, S.-M. Huang, B. Wang, F. Bahrami, B. Xu, J. Franklin, I. Sochnikov, D. E. Graf, G. Xu, Y. Zhao, C. M. Hoffman, H. Lin, D. H. Torchinsky, C. L. Broholm, A. Bansil, F. Tafti, *Phys. Rev. B* **2021**, *103*, 115143.
[42] H. Su, X. Shi, J. Yuan, Y. Wan, E. Cheng, C. Xi, L. Pi, X. Wang, Z. Zou, N. Yu, W. Zhao, S. Li, Y. Guo, *Phys. Rev. B* **2021**, *103*, 165128.
[43] S. K. Dhar, S. M. Pattalwar, *J. Magn. Magn. Mater.* **1996**, *152*, 22.
[44] T. Ng, Y. Luo, J. Yuan, Y. Wu, H. Yang, L. Shen, *Phys. Rev. B* **2021**, *104*, 014412.
[45] D. Tay, T. Shang, P. Puphal, E. Pomjakushina, H. R. Ott, T. Shiroka, *Phys. Rev. B* **2020**, *102*, 241109.
[46] J. Gaudet, H.-Y. u. Yang, S. Baidya, B. Lu, G. Xu, Y. Zhao, J. A. Rodriguez-Rivera, C. M. Hoffmann, D. E. Graf, D. H. Torchinsky, P. Nikolic, D. Vanderbilt, F. Tafti, C. L. Broholm, *Nat. Mater.* **2021**, *20*, 1650.
[47] W. Liu, J. Zhao, F. Meng, A. Rahman, Y. Qin, J. Fan, L. Pi, Z. Tian, H. Du, L. Zhang, Y. Zhang, *Phys. Rev. B* **2021**, *103*, 214401.

[48] P. Puphal, V. Pomjakushin, N. Kanazawa, V. Ukleev, D. J. Gawryluk, J. Ma, M. Naamneh, N. C. Plumb, L. Keller, R. Cubitt, E. Pomjakushina, J. S. White, *Phys. Rev. Lett.* **2020**, *124*, 017202.

[49] H. Y. Yang, B. Singh, B. Lu, C. Y. Huang, F. Bahrami, W. C. Chiu, D. Graf, S. M. Huang, B. Wang, H. Lin, D. Torchinsky, A. Bansil, F. Tafti, *APL Mater.* **2020**, *8*, 011111.

[50] J. F. Wang, Q.-X. Dong, Z.-P. Guo, M. Lv, Y.-F. Huang, J.-S. Xiang, Z.-A. Ren, Z.-J. Wang, P. J. Sun, G. Li, *Phys. Rev. B* **2022**, *105*, 144435.

[51] C. Li, J. Zhang, Y. Wang, H. Liu, Q. Guo, E. Rienks, W. Chen, F. Bertran, H. Yang, D. Phuyal, H. Fedderwitz, B. Thiagarajan, M. Dendzik, M. H. Berntsen, Y. Shi, T. Xiang, O. Tjernberg, *Nat. Commun.* **2023**, *14*, 7185.

[52] E. Cheng, L. Yan, X. Shi, R. Lou, A. Fedorov, M. Behnami, J. Yuan, P. Yang, B. Wang, J.-G. Cheng, Y. Xu, Y. Xu, W. Xia, N. Pavlovskii, D. C. Peets, W. Zhao, Y. Wan, U. Burkhardt, Y. Guo, S. Li, C. Felser, W. Yang, B. Büchner, *Nat. Commun.* **2024**, *15*, 1467.

[53] X. He, Y. Li, H. Zeng, Z. Zhu, S. Tan, Y. Zhang, C. Cao, Y. Luo, *Sci. China Phys. Mech. Astron.* **2023**, *66*, 237011.

[54] R. Lou, A. Fedorov, L. X. Zhao, A. Yaresko, B. Buechner, S. Borisenko, *Phys. Rev. B* **2023**, *107*, 035158.

[55] S. Ahn, E. J. Mele, H. Min, *Phys. Rev. B* **2017**, *95*, 161112.

[56] D. Xiao, M.-C. Chang, Q. Niu, *Rev. Mod. Phys.* **2010**, *82*, 1959.

[57] G. Y. Guo, H. Ebert, *Phys. Rev. B* **2010**, *50*, 10377.

[58] G. Kresse, J. Furthmüller, *Phys. Rev. B* **1996**, *54*, 11169.

[59] G. Kresse, D. Joubert, *Phys. Rev. B* **1999**, *59*, 1758.

[60] P. E. Blöchl, *Phys. Rev. B* **1994**, *50*, 17953.

[61] J. P. Perdew, K. Burke, M. Ernzerhof, *Phys. Rev. Lett.* **1996**, *77*, 3865.